

# The Growth of Black Holes from Population III Remnants in the Renaissance Simulations

Britton D. Smith<sup>1\*</sup>, John A. Regan<sup>2†</sup>, Turlough P. Downes<sup>2</sup>, Michael L. Norman<sup>1,3</sup>, Brian W. O’Shea<sup>4,5,6,7</sup> & John H. Wise<sup>8</sup>

<sup>1</sup>San Diego Supercomputer Center, University of California, San Diego, 10100 Hopkins Drive, La Jolla, CA 92093

<sup>2</sup>Centre for Astrophysics & Relativity, School of Mathematical Sciences, Dublin City University, Glasnevin, Ireland

<sup>3</sup>Center for Astrophysics and Space Sciences, University of California, San Diego, 9500 Gilman Dr, La Jolla, CA 92093

<sup>4</sup>National Superconducting Cyclotron Laboratory, Michigan State University, MI, 48823, USA

<sup>5</sup>Department of Physics and Astronomy, Michigan State University, MI, 48823, USA

<sup>6</sup>Department of Computational Mathematics, Science and Engineering, Michigan State University, MI, 48823, USA

<sup>7</sup>Joint Institute for Nuclear Astrophysics - Center for the Evolution of the Elements, USA

<sup>8</sup>Center for Relativistic Astrophysics, Georgia Institute of Technology, 837 State Street, Atlanta, GA 30332, USA

3 March 2022

## ABSTRACT

The formation of stellar mass black holes from the remnants of Population III stars provides a source of initial black hole seeds with the potential to grow into intermediate or, in rare cases, possibly super-massive black holes. We use the *Renaissance* simulation suite to follow the growth of over 15,000 black holes born into mini-haloes in the early Universe. We compute the evolution of the black holes by post-processing individual remnant Population III star particles in the *Renaissance* simulation snapshots. The black holes populate haloes from  $10^6 M_{\odot}$  up to  $10^9 M_{\odot}$ . We find that all of the black holes display very inefficient growth. On average, the black holes increase their initial mass by a factor  $10^{-5}$ , with the most active black holes increasing their mass by approximately 10%. Only a single black hole experiences any period of super-Eddington accretion, but the duration is very short and not repeated. Furthermore, we find no correlation of black hole accretion with halo mass in the mass range sampled. Within most haloes, we identify clumps of cool, dense gas for which accretion rates would be high, but instances of black holes encountering these clumps are rare and short-lived. Star formation competes with black hole growth by consuming available gas and driving down accretion rates through feedback. We conclude that the black holes born from Population III remnants do not form a significant population of intermediate mass black holes in the early Universe and will need to wait until later times to undergo significant accretion, if at all.

**Key words:** Cosmology: theory – large-scale structure – first stars, methods: numerical

## 1 INTRODUCTION

The existence of supermassive black holes (SMBHs) in the first billion years of the Universe presents a significant challenge to our understanding of the formation of the first compact objects in our Universe. The earliest SMBHs observed have masses upwards of a billion solar masses (e.g. Fan et al. 2006; Mortlock et al. 2011; Venemans et al. 2013; Wu et al. 2015; Bañados et al. 2018). The means by which black holes could grow to be so massive so quickly represents a serious theoretical challenge. Beginning with the spherical accretion model, the maximum accretion rate for a black hole can

be expressed as

$$M(t) = M_0 \exp\left(\frac{1 - \epsilon_r}{\epsilon_r} \frac{t}{t_{\text{Edd}}}\right), \quad (1)$$

where  $t_{\text{Edd}} = 0.45$  Gyr and  $\epsilon_r$  is the radiative efficiency. For a “standard” radiative efficiency of  $\epsilon_r \sim 0.1$  and a black hole seed mass of  $M_0 = 10^2 M_{\odot}$ , it takes nearly 1 Gyr to grow to  $M(t) \sim 10^9 M_{\odot}$ . At present, there exist two potential origin stories for the SMBHs that inhabit the centres of massive galaxies and shine as bright quasars. The seeds of massive black holes may have been “light” ( $\sim 10 - 1000 M_{\odot}$ ), beginning as the remnants of the first stars (e.g. Madau & Rees 2001) or from the core collapse of dense stellar clusters (Gürkan et al. 2004, 2006; Devecchi & Volonteri 2009; Katz et al. 2015). Alternatively, the seeds may have been “heavy” ( $\sim 10^3 - 10^5 M_{\odot}$ ), being the end product of supermassive star formation (e.g., Hosokawa et al. 2013a,b; Woods et al. 2017). The first (Population III) stars in the Universe form out of

\* E-mail: bds006@sdsc.edu

† Marie Skłodowska-Curie Fellow

metal-free gas with  $\text{H}_2$  as the primary coolant. Within a few hundred million years after the Big Bang, Population (Pop) III stars will begin forming in  $10^6 M_\odot$  haloes (Tegmark et al. 1997; Yoshida et al. 2003). The inefficiency of  $\text{H}_2$  as the sole gas coolant results in initial stellar masses that are tens to hundreds of times more massive than the sun (Bromm et al. 1999; Abel et al. 2000, 2002a; Bromm et al. 2002; O’Shea & Norman 2007a; Turk et al. 2009a; Clark et al. 2011; Hirano et al. 2014). This range of masses provides multiple pathways for black hole formation, including core-collapse supernovae or hypernovae ( $11 M_\odot \leq M \leq 40 M_\odot$ ; Woosley & Weaver 1995; Nomoto et al. 2006) and direct formation ( $40 M_\odot \leq M \leq 140 M_\odot$  and  $M > 260 M_\odot$ ; Heger & Woosley 2002), leading to a population of light seeds that have been implanted into the building blocks of galaxies. The expected large number density of Pop III stars in the early Universe (Trenti & Stiavelli 2009; Crosby et al. 2013) makes them natural candidates for the seeds of SMBHs.

Accretion onto Pop III remnants has been investigated as a pathway for forming SMBHs through both analytical (e.g. Madau & Rees 2001) and semi-analytical mechanisms (e.g. Tanaka & Haiman 2009; Pezzulli et al. 2016). Even if only a small fraction of the Pop III remnant black holes grow at the Eddington rate, it would be enough to seed the entire population of SMBHs observed in the Universe. Detailed numerical simulations have also been used to study the initial conditions surrounding the black hole which forms from a Pop III star. These simulations take into account the radiation field generated by the Pop III star, the formation of an HII region surrounding the star, and any associated supernova explosion. The stellar radiation and supernova successfully evacuate the gas from the host halo, resulting in black holes that are “born starving” (Whalen et al. 2004; O’Shea et al. 2005; Johnson & Bromm 2007; Milosavljević et al. 2009). Simulations following the evolution for up to 200 Myr after initial formation find that these black holes continue to experience no significant growth (Alvarez et al. 2009). However, these simulations did not have sufficient dynamic range to follow the subsequent mergers of remnant mini-haloes into larger atomic cooling haloes in which the black holes may be able to experience significant accretion events.

Jeon et al. (2012) simulate the growth of  $100 M_\odot$  black holes from Pop III remnants with and without feedback from the accreting black hole. In the case of no feedback, they find that growth is negligible for  $\sim 80$  Myr until the halo reaches the atomic cooling limit, at which time growth increases significantly. When feedback is included, Jeon et al. (2012) find that growth remains insignificant through the end of the simulation at  $z = 10$ . However, Volonteri et al. (2015) claim that the early bottleneck in growth might also be alleviated by short periods of super-Eddington growth that allow black holes to grow by several orders of magnitude in only 10 Myr. If a black hole is able to migrate into an environment where super-critical accretion becomes possible, then growth to a SMBH mass within the timescale of approximately 500 Myr becomes possible (Lupi et al. 2016; Valiante et al. 2016; Pezzulli et al. 2017; Pacucci et al. 2017).

Heavy seeds emerge from a rarer, more exotic channel where unusually high accretion rates lead to the formation of a super-massive star (Begelman et al. 2006, 2008; Schleicher et al. 2013; Hosokawa et al. 2013b; Woods et al. 2017; Haemmerlé et al. 2018). These direct collapse black holes (DCBHs) are thought to form in pristine atomic cooling haloes where  $\text{H}_2$  formation has been suppressed preventing the formation of smaller Pop III stars (Wise et al. 2008; Regan & Haehnelt 2009a,b; Agarwal et al. 2012, 2013; Becerra et al. 2015; Latif et al. 2013b,a; Regan et al. 2014; Agar-

wal et al. 2016; Regan et al. 2016, 2017). DCBH scenarios have the distinct advantages of starting from much larger masses than light seeds and also existing in environments where significantly more fuel is likely to be present (Hosokawa et al. 2016; Nakauchi et al. 2017). However, the very existence of supermassive stars is debated and furthermore it is not clear whether the DCBH scenario can provide a sufficient number density of black holes to explain the existence of all SMBHs.

In this work, we seek to quantify the range of possibilities for the Pop III light seed scenario in the early Universe. We follow the growth of 15,000 black holes in the *Renaissance* simulations (Xu et al. 2013a, 2014; O’Shea et al. 2015; Xu et al. 2016b,a) over approximately 300 Myr, three orders of magnitude in halo mass, and three different large-scale galactic environments. We supplement this data set with 12 Pop III remnants from the *Pop2Prime* simulations (Smith et al. 2015), which have superior mass, spatial, and time resolution. Both of these sets of simulations follow the formation and evolution of individual Pop III stars using radiation-hydrodynamics in a cosmological context. We examine the growth rates of the total black hole population and identify the commonalities of those that grow the most. We then focus on the halo with the most black holes. Finally, we study how the black hole growth rate is regulated by star formation. The layout of the paper is as follows. In Section 2, we describe the simulations used in this work. In Section 3.1, we discuss the methods for modeling black hole growth. In Section 4, we present the results of the investigations described above. Finally, we conclude with a discussion and summary in Section 5.

## 2 SIMULATION SUITES

All simulations analyzed in this work were performed with the open-source, adaptive mesh-refinement + N-body code, Enzo (Bryan et al. 2014). Enzo has been used extensively to simulate high-redshift structure, including the formation of Pop III stars (Abel et al. 2002b; O’Shea et al. 2005; O’Shea & Norman 2007b, 2008a; Turk et al. 2009b, 2010, 2011a, 2012), low-metallicity stars (Smith & Sigurdsson 2007; Smith et al. 2009a; Meece et al. 2014; Smith et al. 2015), and the first galaxies (Wise et al. 2012; Wise et al. 2012a; Xu et al. 2013b; Wise et al. 2014; Chen et al. 2014a). The two suites of simulations used here are described below.

### 2.1 Renaissance Simulations

The Renaissance Simulations have been well detailed previously in the literature (Xu et al. 2013a, 2014; Chen et al. 2014b; Ahn et al. 2015; O’Shea et al. 2015; Xu et al. 2016a,b), and here we only summarize the simulation characteristics relevant to this study. All of the Renaissance simulations were carried out in a comoving volume of  $(40 \text{ Mpc})^3$ , created with the MUSIC (Hahn & Abel 2011) initial conditions generator. The cosmological parameters were set using the 7-year WMAP  $\Lambda\text{CDM}+\text{SZ}+\text{LENS}$  best fit (Komatsu et al. 2011b):  $\Omega_m = 0.266$ ,  $\Omega_\Lambda = 0.734$ ,  $\Omega_b = 0.0449$ ,  $h = 0.71$ ,  $\sigma_8 = 0.81$  and  $n = 0.963$ . First, an exploratory simulation with  $512^3$  particles ( $1.7 \times 10^7 M_\odot$  per dark matter particle) was run to  $z = 6$ . Three regions of interest were then selected for re-simulation at higher resolution, namely a rare-peak region, a normal region and a void region. To generate the three regions the initial, lower resolution, volume was smoothed on a physical scale of 5 comoving Mpc, and regions of high  $(\langle \delta \rangle \equiv \langle \rho \rangle / (\Omega_M \rho_C) - 1 \sim 0.68)$  -

the rare peak; average ( $\langle\delta\rangle \sim 0.09$ ) - the normal region; and low ( $\langle\delta\rangle \sim -0.26$ ) - the void region. The comoving volumes of the three regions were 133.6, 220.5 and 220.5  $\text{Mpc}^3$ , respectively. Each simulated region was then re-initialized with a further three nested grids for an effective resolution of  $4096^3$  and a dark matter particle resolution of  $2.9 \times 10^4 M_\odot$  within the high-resolution region. During the simulation, further adaptive refinement was allowed up to a maximum 12 levels, leading to a maximum spatial resolution of 19 comoving pc (1.2 proper parsecs at  $z = 15$ ). The simulations were evolved to a final redshift  $z = 15, 11.6$  and  $9.9$  for the Rare-Peak, Normal and Void realisation respectively. The halo mass function is well-resolved down to  $2 \times 10^6 M_\odot$  (70 particles per halo), and at the ending redshift, the three realisations contained a total of 822, 758, 458 galaxies having at least 1,000 particles ( $M_{\text{vir}} \simeq 2.9 \times 10^7 M_\odot$ ) and  $\sim 15,000$  Pop III remnant black holes (see Table 1).

The simulations include both self consistent Pop III and metal-enriched star formation (Pop II) at the maximum refinement level and capture star formation in haloes as small as  $3 \times 10^6 M_\odot$  (Xu et al. 2013a). Pop III star formation is selected if the metallicity is less than  $10^{-4}$  of the solar fraction in the highest density cell with metal-enriched star formation proceeding otherwise. The functional form of the IMF is a power-law with a slope of -1.3 with an exponential cutoff above a characteristic mass of  $40 M_\odot$ . The operational mass range of the IMF is  $1 M_\odot \leq M \leq 300 M_\odot$  (see Wise et al. (2012b) for additional details.) Stellar feedback uses the MORAY radiative transport framework (Wise & Abel 2011) for H ionizing photons. Lyman-Werner (LW) radiation that dissociates  $\text{H}_2$  is modeled using an optically thin, inverse square law profile, centered on all star particles. At the end of their main-sequence lifetimes, Pop III stars in the mass range,  $11 M_\odot \leq M \leq 40 M_\odot$ , explode as core-collapse supernova with total energies and metal yields calculated by Nomoto et al. (2006). Pop III stars in the mass range  $140 M_\odot \leq M \leq 260 M_\odot$  explode as pair-instability supernova (PISN) with total energy of  $\sim 6 - 100 \times 10^{51}$  erg over the PISN mass range and metal yields calculated by Heger & Woosley (2002). For Pop III stars outside of the above mass ranges ( $40 M_\odot < M < 140 M_\odot$  and  $M > 260 M_\odot$ ), no feedback is added after the main-sequence lifetime. The ionization states of hydrogen and helium are followed with a 9-species primordial non-equilibrium chemistry and cooling network (Abel et al. 1997), supplemented by metal-dependent cooling tables (Smith et al. 2009b). No  $\text{H}_2$  self-shielding is included in the simulations as the densities at which it becomes relevant are not fully resolved by the simulations. A LW background radiation field is also included to model radiation from stars which are not within the simulation volume (Wise et al. 2012). In the high density region of the rare-peak simulation, the LW radiation from stars dominates over the background. Although the simulations cannot follow Pop III star formation in haloes below  $3 \times 10^6 M_\odot$ , star formation is suppressed by the LW background in such haloes (Machacek et al. 2001; Wise & Abel 2007; O’Shea & Norman 2008b). Finally, we note the existence of multiple versions of each of these three simulations in the literature. The variations were run to different redshifts and used slightly different methods for calculating the global Lyman-Werner radiation field. For clarity, we list the simulations used here in Table 1 by the names given to them in the upcoming public data release along with the reference of their first appearance.

## 2.2 Pop2Prime Simulations

We supplement the *Renaissance* simulations with an extension of the simulation presented in Smith et al. (2015), referred to here as

**Table 1.** Simulation Summary

Simulation <sup>a</sup>	$V_{\text{hr}}^b$ [(Mpc com.) <sup>3</sup> ]	$z_f^c$	$N_{\text{black holes}}^d$	Ref. <sup>e</sup>
Rare-Peak_LWB	133.6	15.0	6518	1
Normal_BG1	220.5	11.6	6225	2
Void_BG1	220.5	9.9	2487	3
Pop2Prime	0.004	10*	12	4

(a) the simulation name; (b) volume of the high resolution region; (c) the final redshift of the simulation; (d) the total number of Pop III remnant black holes at the final redshift. \* - after  $z = 11.83$ , this simulation was continued to  $z = 10$  with star formation turned off; (e) publication of first appearance. 1: O’Shea et al. (2015), 2: Xu et al. (2016b), 3: Xu et al. (2016a), 4: Smith et al. (2015).

the *Pop2Prime* simulation. With significantly higher mass and spatial resolution, the *Pop2Prime* simulation provides some constraint on the dependence of the results on resolution. The *Pop2Prime* simulation uses a 500 comoving kpc/h box, initialized at  $z = 180$  with the MUSIC initial conditions generator with the WMAP 7 best-fit cosmological parameters,  $\Omega_m = 0.266$ ,  $\Omega_\Lambda = 0.732$ ,  $\Omega_b = 0.0449$ ,  $H_0 = 71.0$  km/s/Mpc,  $\sigma_8 = 0.801$ , and  $n_s = 0.963$  (Komatsu et al. 2011a), and using a Eisenstein & Hu (1999) transfer function and second-order Lagrangian perturbation theory. The simulation follows the region around a halo reaching a virial mass of  $1.7 \times 10^7 M_\odot$  at  $z = 10$ . The initial conditions are generated with  $512^3$  grid cells and dark matter particles on the root grid and two additional levels of nested refinement surrounding the target halo, corresponding to a comoving spatial resolution of 0.244 kpc/h, and a baryon (dark matter) mass resolution of  $0.259 M_\odot$  (1.274  $M_\odot$ ).

The *Pop2Prime* simulation includes the formation and feedback from Pop III stars in a manner similar to the *Renaissance* simulations, with the addition of He ionizing radiation (only H ionizing radiation was used in the *Renaissance* simulations) using the MORAY adaptive ray-tracing method and treating LW radiation as optically thin with  $1/r^2$  attenuation. In contrast to the *Renaissance* simulations, which adopt a power-law Pop III IMF, all Pop III stars in *Pop2Prime* are given a mass of  $40 M_\odot$  and end their main-sequence lifetimes (3.86 Myr) in a core-collapse supernova with total energy of  $10^{51}$  erg. Since the original goal of the *Pop2Prime* simulation was to study the collapse and fragmentation of metal-enriched gas, this simulation does not form any Pop II stars. Instead, gas with metallicity greater than  $10^{-4} Z_\odot$  is allowed to collapse until a number density of  $\sim 10^{13} \text{ cm}^{-3}$  is reached, at which time the simulation stops. This occurs at  $z \sim 11.8$  after a total of 12 Pop III stars have formed. The simulation is then carried forward to  $z = 10$ , roughly an additional 100 Myr, with star formation turned off. This serves as an illuminating experiment of the effects of stellar feedback on black hole growth. The *Pop2Prime* simulation uses the same chemistry and cooling machinery as the *Renaissance* simulations, but with the additions of three deuterium species (D,  $\text{D}^+$ , and HD),  $\text{H}_2$  formation on dust grains (described in Meece et al. 2014), and self-shielding of LW radiation using the model of Wolcott-Green et al. (2011).

## 3 ANALYSIS

### 3.1 Black Hole Formation in the Simulations

The simulations discussed here do not contain a subgrid prescription for black hole formation. Regardless of their initial mass, Pop

III star particles are given a negligible mass at the end of their main-sequence lifetimes and do not accrete from their surroundings. They then effectively act as extremely low mass dark matter particles. The simulations continue to update the positions, velocities, and accelerations of these particles due to gravity, so they will be located in approximately the same positions as if they had been evolved fully self-consistently as black holes. We rely on this fact to model the growth of black holes represented by these particle using accretion rates calculated from the local gas conditions within the available simulation snapshots. This is not self-consistent and completely ignores the gravitational force of the black holes on the surrounding material, changes in momentum/trajectory of the particle due to accretion, and radiative feedback from accretion. Nevertheless, this exercise can provide a rough estimate of the evolution of stellar mass black holes in the early universe across different galactic environments. Within the uncertainties created by the first two caveats, the lack of radiative feedback serves to provide an upper limit on the overall black hole growth.

### 3.2 Calculating Black Hole Growth

We compute growth histories for each Pop III star particle expected to form a black hole based on its zero-age main-sequence (ZAMS) mass. Given the initial mass of the star particle, we calculate its initial black hole mass by linearly interpolating from the results of [Woosley & Weaver \(1995, Table 3\)](#) for stars with  $M < 140 M_{\odot}$ . For stars with  $140 M_{\odot} < M \leq 260 M_{\odot}$ , the star has undergone a PISN and so we assume no compact remnant. For stars with  $260 M_{\odot} < M \leq 300 M_{\odot}$  (the upper limit of the Pop III IMF in the *Renaissance* simulations), we set the initial black hole mass to be the mass of the He core using the relation from [Heger & Woosley \(2002, Equation 1\)](#), given by

$$M_{\text{He}} \simeq \frac{13}{24} (M_{*} - 20 M_{\odot}). \quad (2)$$

We model black hole growth as spherical Bondi-Hoyle accretion ([Hoyle & Lyttleton 1941](#); [Bondi 1952](#)), where the growth rate is given by

$$\dot{m}_{B-H} \simeq \frac{\alpha \pi \rho G^2 M_{BH}^2}{\max(|\vec{v}|, c_s)^3}, \quad (3)$$

where  $M$  is the mass of the black hole,  $\rho$  is the gas density surrounding the black hole,  $c_s$  is the local sound speed,  $|\vec{v}|$  is the magnitude of the velocity of the black hole relative to the surrounding material, and  $\alpha$  is a dimensionless boost factor. [Krumholz et al. \(2005\)](#) show that the accretion rate is decreased when the gas has non-zero vorticity, but we ignore this effect to consider the most optimistic growth scenario. The boost factor term was first added to Equation 3 by [Springel et al. \(2005\)](#) to account for underestimation in the gas density in the vicinity of the black hole caused by limited spatial resolution of the simulation. This scale is the Bondi radius, given by

$$r_b = \frac{2GM_{BH}}{c_s^2}, \quad (4)$$

which we do not resolve in our simulations. [Booth & Schaye \(2009\)](#) excellently summarize the subsequent use of the boost factor in proceeding works, noting the commonly adopted constant values of  $\alpha = 100\text{--}300$  (although see [Pelupessy et al. 2007](#); [Kim et al. 2011](#), for alternative approaches to the boost factor). However, [Booth & Schaye \(2009\)](#) argue that values of  $\alpha > 1$  are unphysical when the medium is single-phase and its associated Jeans length is resolved

by the simulation. In the *Pop2Prime* simulations, the Jeans length is resolved explicitly by a minimum of 64 grid cells. In the *Renaissance* simulations, Jeans length-based refinement is not used, but we find that in practice the Jeans length is refined in the vicinity of the black hole particle by at least 4 cells (i.e., the grid cell containing it) roughly 99.9% of the time. [Booth & Schaye \(2009\)](#) argue that boost factors should be used when the medium is expected to be multi-phase and the associated spatial scales are unresolved. The scale of the multi-phase medium is not set by the Jeans length, but instead by the cooling length (the cooling time multiplied by the sound speed) as it forms through thermal instability ([Voit et al. 2017](#); [McCourt et al. 2018](#)). For the circumgalactic medium, [Fielding et al. \(2017\)](#) find that gas is stable against going multi-phase for halo masses below roughly  $10^{11.5} M_{\odot}$ , relating the associated virial temperature to the point in the cooling curve where cooling times become long. In our case, we find that the black hole particles spend the majority of their time in two regimes: hot ( $T \sim 10^{6-7}$  K), underdense ( $n < 10^{-2} \text{ cm}^{-3}$ ) gas that is the product of stellar feedback; and cooler ( $T \sim 10^4$  K), denser ( $10^{-2} \text{ cm}^{-3} < n < 10^2 \text{ cm}^{-3}$ ) gas heated to the virial temperature, but unable to cool further due to its low metallicity. Due to the long cooling times, we expect that in practice the thermal instability will have no impact and hence the gas will be single phase in both these regimes. Therefore, we choose to adopt a constant value of  $\alpha = 1$  (i.e., no boost) in our growth model. Finally, we do not cap the black hole growth rate at the Eddington limit, which is given by

$$\dot{m}_{Edd} = \frac{4\pi GM_{BH} m_p}{\epsilon_r \sigma_T c} \simeq 2.2 \times 10^{-8} \left( \frac{0.1}{\epsilon_r} \right) \left( \frac{M_{BH}}{M_{\odot}} \right) [M_{\odot}/\text{yr}], \quad (5)$$

where  $m_p$  is the proton mass,  $\epsilon_r$  is the radiative efficiency,  $\sigma_T$  is the Thomson cross-section, and  $c$  is the speed of light. Throughout this work, we refer to the Eddington rate assuming  $\epsilon_r = 0.1$ , appropriate for a non-rotating Schwarzschild black hole ([Shakura & Syunyaev 1973](#)). As we show below, instances of near-Eddington accretion are extremely rare. We allow for super-Eddington accretion only to highlight instances where the physical conditions create a situation where it could be possible.

Starting with the first simulation snapshot after which a Pop III star particle has exceeded its main-sequence lifetime, we use Equation 3 to compute the particle’s instantaneous growth rate<sup>1</sup>. Assuming the density of the grid cell decreases negligibly due to accretion by the particle, Equation 3 can be solved analytically to give the black hole’s mass at snapshot  $i + 1$ , given its mass at snapshot  $i$ ,  $M_i$ , and the timestep between snapshots,  $\Delta t$  as

$$M_{i+1} = \frac{M_i}{1 - \frac{\dot{m}_{B-H} \Delta t}{M_i}}. \quad (6)$$

We compute the final mass of each black hole particle by iterating over all available snapshots for each simulation. For the *Renaissance* simulations, the average time between snapshots is roughly 4 Myr. For the *Pop2Prime* simulation, the average time between snapshots is about 0.8 Myr.

## 4 RESULTS

Below, we present the results of growing the Pop III remnant black holes for each simulation to its final snapshot, focusing primarily on

<sup>1</sup> All analysis codes used in this work, including figure-generating scripts, are available as an extension package for the yt analysis code ([Turk et al. 2011b](#)) at [https://github.com/brittonsmith/yt\\_p3bh](https://github.com/brittonsmith/yt_p3bh).



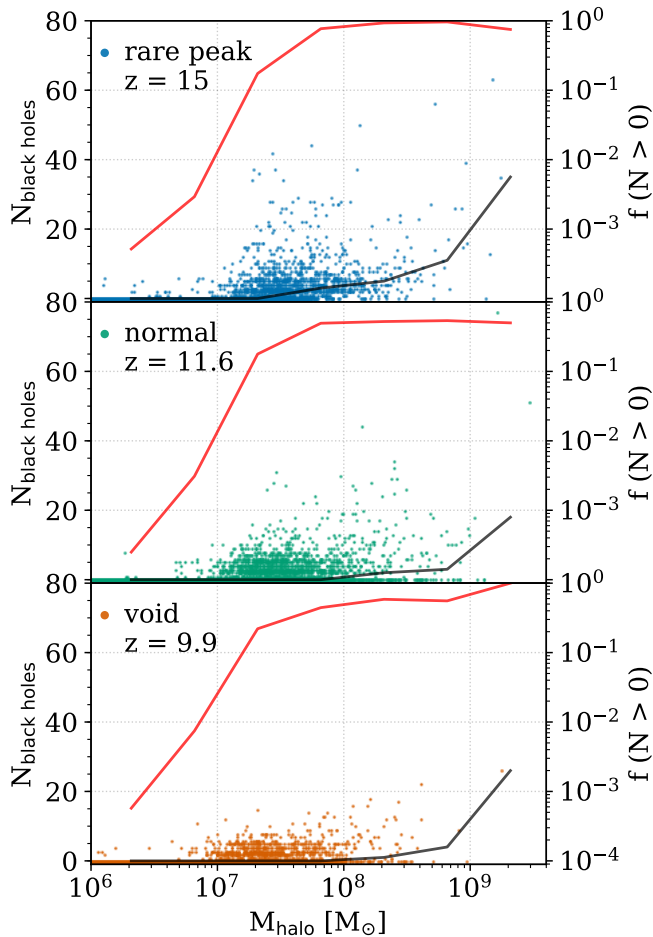


**Figure 1.** Number of black holes in a halo as a function of halo mass for the rare peak (top), normal (middle), and void (bottom) runs of the *Renaissance* simulations. The black line indicates the median in bins of 0.5 dex and the red line shows the fraction of haloes with at least one black hole.

the *Renaissance* simulations. We note that the Rarepeak and Normal simulations were run until a qualitatively similar amount of structure (number of haloes, stars, etc.) had formed, hence the similarity in the number of black holes formed. However, this is not true for the Void simulation, whose final redshift was determined by a prior simulation that was used to create a LW background model for the Void simulation. Unless otherwise stated, the results shown refer to the final output of each simulation. Table 1 lists the final redshift and total number of black holes formed in each simulation.

#### 4.1 Where are the black holes?

In Figure 1, we show the number of black holes as a function of halo mass at the final snapshot of each of the *Renaissance* simulations. Over the three simulations we find that the distribution of black holes is scattered from haloes as small as a few times  $10^6 M_\odot$ , roughly the resolution limit, up to approximately  $10^9 M_\odot$ , the maximum halo mass. The void haloes (bottom panel) show the smallest number of black holes per halo with on average less than one black hole per halo up to  $M_{halo} \sim 10^7 M_\odot$ . The normal and rare haloes show a slightly larger scatter with a handful of haloes having up to 40 black holes per halo up to  $M_{halo} \sim 10^7 M_\odot$ . In all cases, less than roughly 1% of haloes with  $M_{halo} < 10^7 M_\odot$  are populated with Pop III black holes. Above a mass of

$M_{halo} \sim 10^7 M_\odot$ , the number of black holes shows a marked increase in number, especially for the normal and rare peak haloes. This is because at this mass scale atomic haloes form through the merger and accretion of mini-haloes which previously hosted black holes. Xu et al. (2013a) found in their investigation of Pop III stars in the Renaissance simulations that the number of Pop III stars and remnants peaks in haloes with masses of a few  $\times 10^7 M_\odot$  and that the growth in the number of remnants comes mainly from mergers of mini-haloes. They find that Pop III stars form only in haloes with masses between  $4 \times 10^6$  and  $3 \times 10^8 M_\odot$ . Pop III stars found in higher mass haloes appear there via mergers. It is the remnants of these Pop III stars that now populate the more massive atomic cooling haloes. The median line (solid black line in Figure 1) shows a clear increase in the number of black holes in haloes more massive than approximately  $10^8 M_\odot$  due to the effect of mergers. We therefore sample quite well the black hole occupation fraction in haloes up to  $M_{halo} \sim 10^9 M_\odot$ .

#### 4.2 How much do the black holes grow?

In Figure 2, we show histograms of black hole properties, including formation redshift, relative growth, final mass, and maximum instantaneous growth rate. As expected, the black hole formation rate is indicative of the large-scale overdensity associated with each simulation. The landscape of overall black hole growth is notably bleak. Not a single black hole is able to double in size, with the best cases growing by roughly 13% in the Rarepeak. In the less dense galactic environments, the maximal mass growth is even lower, with the best case in the Normal run growing only by 2%, and that of the Void run by just under 1%. In all three cases, the distribution of relative black hole growth is bimodal, with peaks at  $\sim 10^{-15}$  to  $\sim 10^{-13}$  and a broader peak from  $\sim 10^{-8}$  to  $\sim 10^{-3}$ . The distribution of maximum instantaneous growth rates closely resembles the overall relative growth. In all, only a single black hole in the Rarepeak is able to achieve super-Eddington accretion. The overwhelming majority of black holes accrete maximally at less than  $10^{-4}$  of their Eddington rates. Figure 3 shows a probability distribution function of all instantaneous growth rates for all black holes and all snapshots. Only 2-3% of all growth rates exceed  $10^{-4}$  of the Eddington rate the total number of super-Eddington events is just one, i.e., the one black hole that experiences super-Eddington growth does so only once.

The *Pop2Prime* simulation shows a similar bimodal distribution of individual growth rates, albeit with narrower peaks and an overall much smaller range of total values. The two peaks correspond to two distinct physical conditions in which the black holes tend to exist. The lower of the two peaks is from hot, underdense gas associated with stellar feedback. All black holes forming in a supernova event will live in this phase at least once, and likely much longer given the long associated cooling times and continually occurring star formation. The higher peak comes from gas about to form stars, where the medium is slightly denser and heated to roughly the virial temperature. In *Pop2Prime*, the lower peak occurs at a higher growth rate because of the relative weakness of the stellar feedback producing lower temperatures in the hot phase. Haloes in *Pop2Prime*, with masses of only a few hundred thousand  $M_\odot$ , form only 1-2 stars total. These smaller haloes also have lower virial temperatures and central gas densities, thus moving the location of the second peak in Figure 3 to lower accretion rates.

In Figure 4, we plot the relative growth of black holes as a function of their age. For black holes in the bulk of the relative

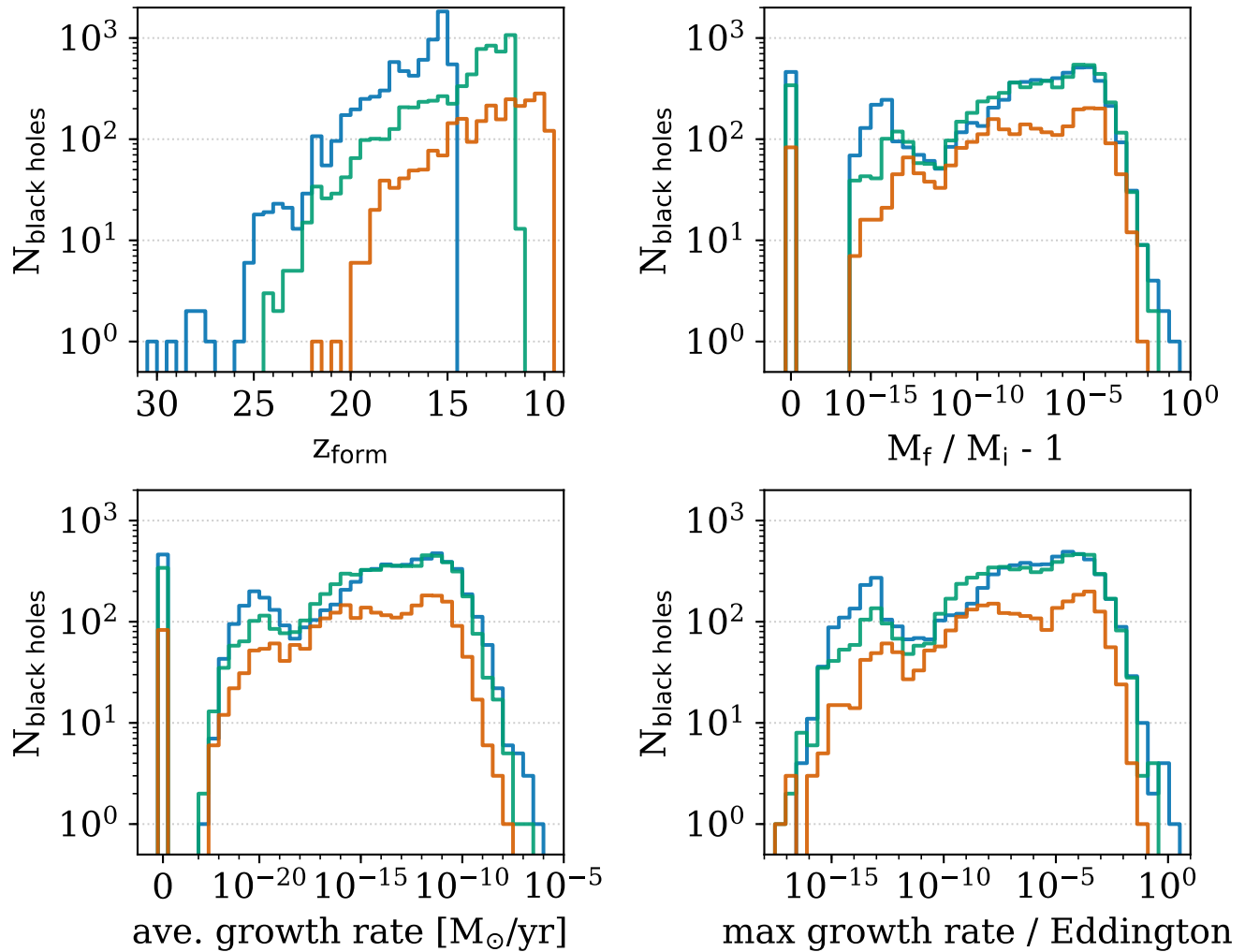


**Figure 2.** Black hole population statistics for the final snapshot of the rare peak (blue,  $z = 15$ ), normal (green,  $z = 11.6$ ), and void (orange,  $z = 9.9$ ) runs of the *Renaissance* simulations. *Top Left Panel:* black hole formation redshift. The drop-off corresponds to the final redshift of each simulation. *Top Right Panel:* relative overall black hole growth. The vast majority of black holes grow by a negligible amount. No black holes are able to increase their mass by more than 10%. *Bottom Left Panel:* average absolute growth rate. *Bottom Right Panel:* maximum instantaneous growth rate, as a fraction of the Eddington rate, achieved at any point during the simulation.

growth distribution (Figure 2, top-right panel), there is effectively no relation between overall growth and age apart from the lack of older black holes at the lowest values of relative growth. The black holes showing the most growth are relatively young, with ages less than about 50 Myr. In Figure 5, we show the individual growth histories for all black holes growing by at least 0.5%. In all but one case, these black holes reach  $> 90\%$  of their final mass in less than 10 Myr. There are 9 black holes in the Rarepeak realisation that grow by at least 0.5%, 4 in the Normal, and only one in the Void. Of the 14 black holes shown here, 6 reach accretion rates of at least one quarter of Eddington, with one reaching 2.5 times Eddington. In all cases, this strong growth lasts for only a single snapshot, and is therefore likely overestimated. Not surprisingly, all 14 of these black holes are in the mass windows where formation occurs without a preceding supernova, i.e.,  $40 M_{\odot} < M < 140 M_{\odot}$  and  $M > 260 M_{\odot}$ . These stellar mass ranges correspond to initial black hole masses of  $16.6 M_{\odot} < M < 65 M_{\odot}$  and  $M > 130 M_{\odot}$ . Apart from this initial period of super critical growth, no black holes are able to accrete at rates exceeding the Eddington

limit, with most accreting at rates many orders of magnitude below the Eddington rate.

Finally, in Figure 6 we plot the specific growth rate (average growth rate divided by initial mass) for all black holes as a function of host halo mass. Within the mass range tracked by the *Renaissance* simulations ( $10^6 M_{\odot} < M_{halo} < 10^9 M_{\odot}$ ), we see no evidence of the larger gas reservoirs of more massive haloes aiding in black hole growth, except to the extent that higher mass haloes show a scarcity of the most slowly growing black holes. This finding appears to be in agreement with the isolated galaxy simulations of Pelupessy et al. (2007), who find no instances super-Eddington growth in haloes up to  $10^{10} M_{\odot}$ . The cosmological simulations of Habouzit et al. (2017), which include black hole growth with feedback in a 10 Mpc comoving box, also find very limited accretion at high redshift. Similar to this work, the distribution of accretion rates in Habouzit et al. (2017) also show a peak around  $10^{-5}$  of the Eddington rate, although their larger box size and lower final redshift (at the cost of lower resolution) are able to capture more instances of much higher accretion rates.

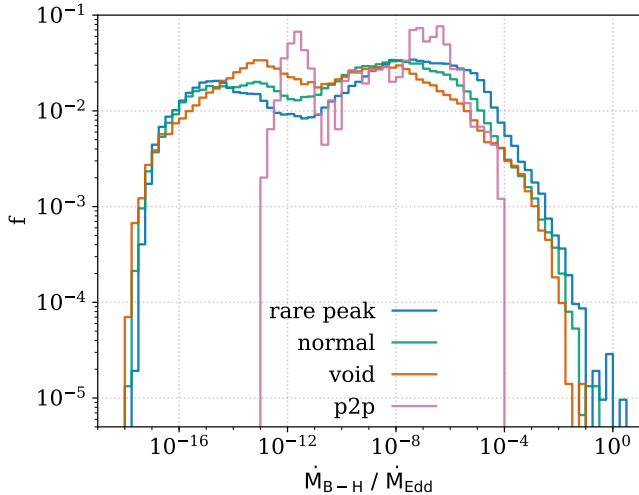


**Figure 3.** Probability distribution function of all instantaneous growth rates for all black holes over all times for all simulations. Growth rates are shown as a fraction of the Eddington rate. For the *Pop2Prime* simulation (p2p above), the period of time where star formation is turned off is not shown as this is unphysical.

The global statistics shown in Figures 4, 5 and 6 support the conclusion that light seeds, born from Pop III remnant black holes do not grow efficiently by accretion in haloes up to  $M_{\text{halo}} \sim 10^9 M_{\odot}$ . Next, we examine a single halo in detail to understand why these black holes are unable to grow.

### 4.3 Why do the black holes not grow?

As we have seen the black hole accretion rate shows no marked increase as a function of time or halo mass. To further understand the evolution of Pop III remnant black holes we examine in detail the halo with the most black holes, coming from the Normal run with a total of 77 black holes at the final output. In Figure 7, we plot the halo’s large-scale gas distribution with the effective “accretability” of the central, dense gas shown in the bottom panel. Here, we define the accretability as the ratio of the Bondi-Hoyle rate to the Eddington rate, divided by black hole mass. If we ignore the relative motion term in Equation 3 and consider only the sound speed of the gas, the above quantity is independent of black hole mass and is simply a measure of the gas properties. Accretability has units of  $M_{\odot}^{-1}$ , meaning that for an accretability of  $0.1 M_{\odot}^{-1}$ , a  $1 M_{\odot}$  black hole would accrete at 0.1 of Eddington and a  $10 M_{\odot}$  black hole would accrete at Eddington. Regions of high accretability are clearly associated with dense gas, but the converse of that statement is not necessarily true. Interestingly, high accretability clumps do not appear to be centrally concentrated.

In the bottom panel of Figure 7, we overplot the locations of all black holes in the inner halo, ( $r < 0.25 r_{\text{vir}}$ ). We use the `yt` clump finder (Smith et al. 2009b; Turk et al. 2011b) to identify all topologically disconnected regions with accretability of at least  $10^{-3} M_{\odot}^{-1}$ . We choose this value as it is the minimum value for a few hundred  $M_{\odot}$  black hole (the maximum mass considered in this work) to approach the Eddington limit. To remove projection effects, the black holes shown in Figure 7 are colored by the distance to the nearest gas clump with accretability of at least  $10^{-3} M_{\odot}^{-1}$ . The closest encounter between a black hole and a highly accretable clump is roughly 30 pc, but on average, black holes are many hun-

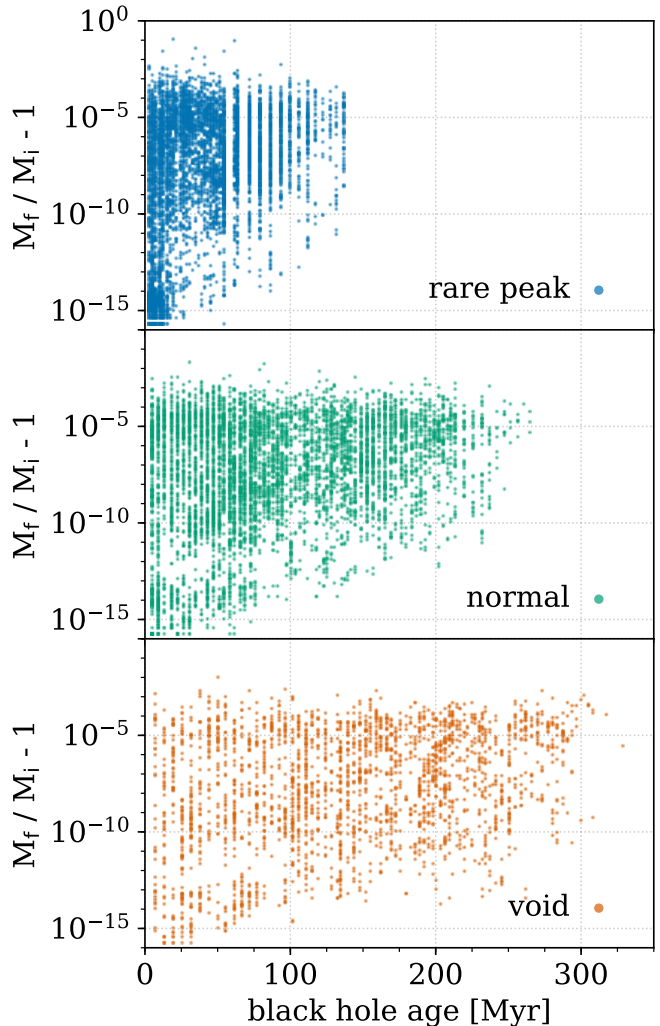


**Figure 4.** Relative black hole growth as a function of black hole age, where  $M_i$  and  $M_f$  are the initial and final masses, respectively. No strong trend of black hole growth versus age exists. However, black holes with the most and least growth are generally young ( $\lesssim 50$  Myr).

dreds of pc away from these clumps. In this snapshot, no black holes are within such a clump.

In order for a black hole to experience high growth rates, it must intersect with a high accretability clump at some time. To quantify the frequency of interactions between black holes and clumps, we measure the distances from each black hole to the edge of the nearest clump over the history of this halo and all of its progenitors. We construct a merger-tree of this halo using the `consistent-trees` merger-tree code (Behroozi et al. 2013b). We use the `ytree` code (Smith 2018) to walk the tree, interface with `yt`, and run the clump finding algorithm as described above for all progenitors of the halo in question. In Figure 8, we plot the distribution of distances between black holes and nearest clumps as a function of time, with the median value for black holes within one quarter of the virial radius shown in black. Throughout most of the halo’s history, black holes remain on average a few hundred pc away from clumps in which they could grow rapidly, with the closest black holes still tens of pc away. In total, we note 10 occasions of black holes existing in highly accretable clumps, with their details shown in Table 2. Half of these ten occurrences consist of

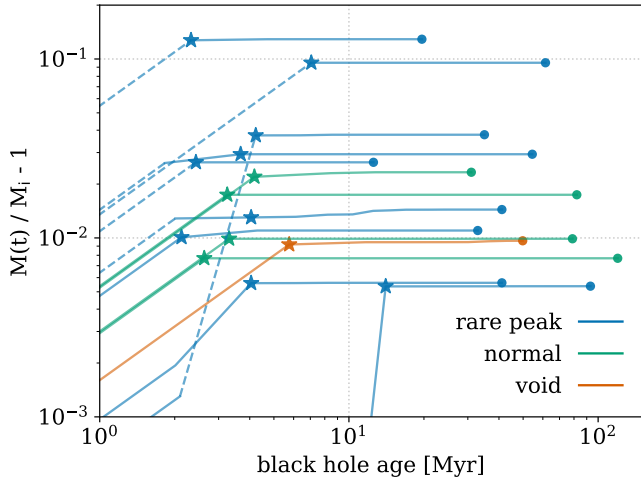


**Figure 5.** Relative black hole mass as a function of age for all black holes with total relative growth of at least 0.005. Stars indicate the time when the black hole has accomplished 90% of its total growth and the circles denote its final mass and age. Dashed lines indicate periods of black hole growth of at least 0.25 of the Eddington rate.

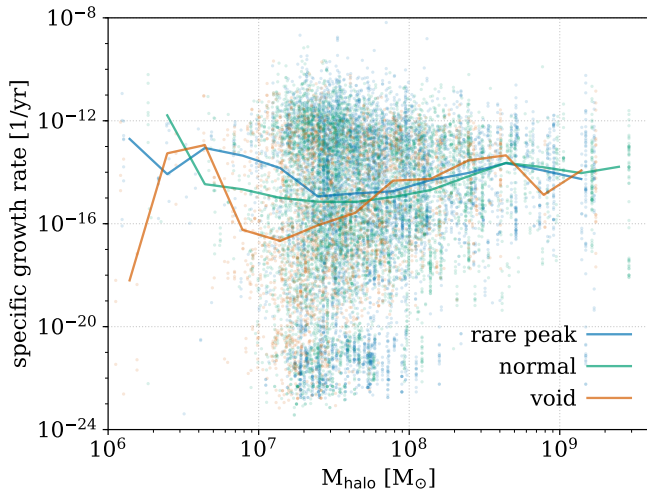


**Figure 6.** Specific black hole growth rate as a function of halo mass, where specific growth rate is defined as  $(M_f - M_i) / (M_i \times \text{age})$ . Solid lines indicate median number of black holes per halo in mass bins of 0.25 dex. We find no correlation of black hole growth with halo mass up to  $M_{\text{halo}} \sim 10^9 M_{\odot}$ .

a new black hole in the direct formation mass range. Two others in the same mass range are only 2.5 Myr old. The maximum time spent inside a clump was just over 3 Myr with an average accretion rate of  $10^{-8} M_{\odot}/\text{yr}$ , and in all cases the accretion rate was sub-Eddington. Black holes appear to have a difficult time remaining in clumps, either because they migrate out or because those clumps are consumed or destroyed. If the latter is true, then the most likely cause is star formation, as highly accretable gas is cold and dense.

We use the *Pop2Prime* simulation to test the hypothesis that black hole growth is regulated by star formation and feedback. As described in §2.2, the *Pop2Prime* simulation is an extremely high resolution simulation in a very small volume and hence only 12 black holes exist by  $z \sim 12$ . At  $z \simeq 11.8$ , we turn off star formation, but allow the simulation to evolve in every other respect. The

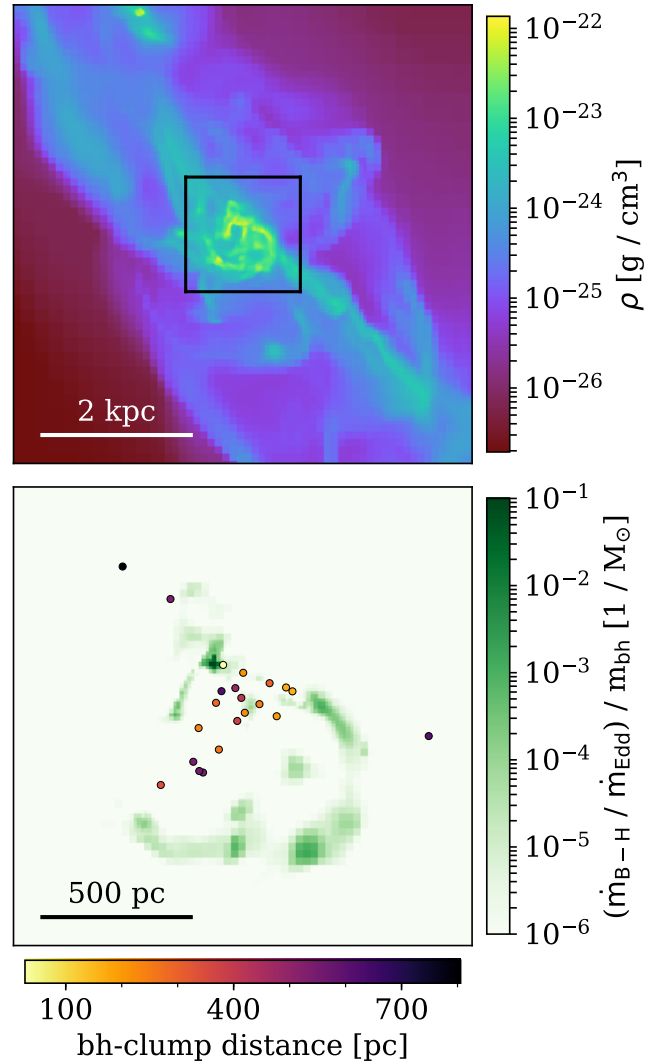


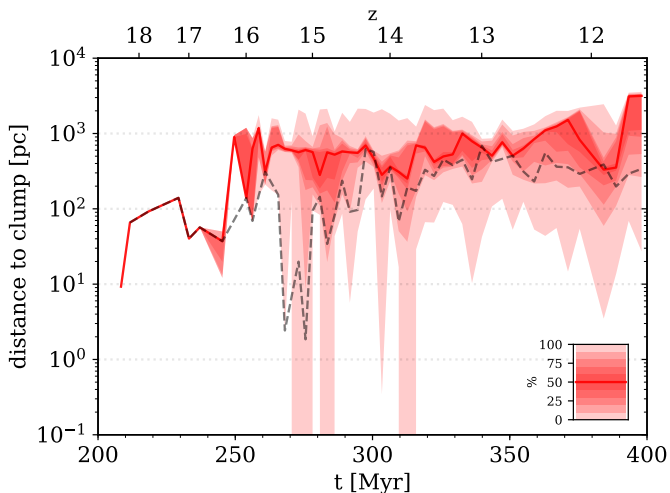
**Figure 7.** *Top Panel:* projection of mass-weighted mean density for the halo with the most black holes ( $M_{\text{halo}} = 1.6 \times 10^9 M_{\odot}$ ,  $n_{\text{BH}} = 77$ ). The size of the projected region denotes the halo’s virial radius of 3.4 kpc. *Bottom Panel:* mass-weighted projection of gas accretability, defined as the ratio of Bondi-Hoyle to Eddington, divided by black hole mass. For example, a value of  $0.1 M_{\odot}^{-1}$  would allow a  $1 M_{\odot}$  black hole to accrete at 0.1 Eddington and a  $10 M_{\odot}$  black hole to accrete at Eddington. The projected region is 0.25 of the virial radius. Circles indicate the locations of black holes, with colors denoting the distance to the nearest gas clump with an accretability of at least  $10^{-3} M_{\odot}^{-1}$ .

growth rates for all 12 black holes are shown in Figure 9. After star formation is disabled, the mean growth rate increases by roughly two orders of magnitude in 100 Myr. However, more notably, the growth rates of the oldest black holes, whose haloes have had much more time to reassemble, have increased by a much greater degree. Jeon et al. (2014) find that  $\sim 10^5 M_{\odot}$  mini-haloes can take more than 100 Myr to reassemble, so the low growth rates of the latest forming black holes are not surprising. The top-right panel of Figure 9 indicates that it is the increase in density which drives the enhancement of black hole growth after star formation has ceased. The sound speed has also dropped considerably at this time, but this turns out to be unimportant as the gas/particle relative velocity remains roughly 10 km/s. With a self-consistent treatment of



**Table 2.** Black holes interacting with clumps in Figure 8.

Particle ID <sup>a</sup>	$z^b$	$m_{\text{bh}}^c$ [ $M_{\odot}$ ]	age <sup>d</sup> [Myr]	$\dot{m}_{\text{bh}}^e$ [ $M_{\odot} / \text{yr}$ ]	$\dot{m}_{\text{bh}}^f / \dot{m}_{\text{Edd}}$	$\Delta t^g$ [Myr]	$\Delta m^h$ [ $M_{\odot}$ ]
618050081	15.2	46.053	0.00	1.167e-07	1.152e-01	2.547	2.973e-01
618051131	15.2	48.921	0.00	1.878e-07	1.745e-01	2.547	4.784e-01
618048385	15.2	28.510	0.00	8.338e-08	1.329e-01	2.547	2.124e-01
"	15.1	28.722	2.54	5.292e-08	8.374e-02	2.587	1.369e-01
618049168	15.2	27.457	0.00	5.915e-08	9.793e-02	2.547	1.507e-01
"	15.1	27.607	2.54	2.032e-08	3.346e-02	2.587	5.258e-02
618062820	15.1	17.272	0.00	4.052e-08	1.066e-01	2.587	1.048e-01
617970154	14.8	8.547	33.88	1.957e-09	1.041e-02	2.712	5.307e-03
617970240	13.8	42.303	67.36	5.976e-08	6.422e-02	3.195	1.910e-01
617977875	13.8	17.271	63.07	7.217e-09	1.899e-02	3.195	2.306e-02

(a) the particle id of the black hole; (b) redshift of interaction; (c) black hole mass; (d) black hole age; (e) Bondi-Hoyle accretion rate; (f) fraction of Eddington accretion rate; (g) time between current and next snapshots; (h) mass accreted in  $\Delta t$ .**Figure 8.** Distribution of distances between a black hole and a high accretability gas clump (greater than  $10^{-3} M_{\odot}^{-1}$ ) for all progenitor haloes of the halo hosting the most black holes (shown in Figure 7.) Where the shaded region extends to the bottom of the figure, some black holes exist within high accretion rate clumps. See Table 2 for a list of all instances of black holes within clumps. Values shown in red correspond to all black holes within a halo’s virial radius. The black, dashed line denotes the median separation for black holes within 0.25 of the virial radius.

black hole formation and evolution (i.e., not what we have done here), black holes should eventually sink to the center of the halo due to dynamical friction, although this will be slow because of their low masses. Indeed, [Sugimura et al. \(2018\)](#) find that dynamical friction is unable to transport black holes formed in mini-halos into the inner, gas-rich regions of atomic cooling halos. As galaxies grow larger, they will be more able to co-locate black holes and accretable gas. Regardless, this provides strong evidence that the ability of stellar feedback to destroy cold, dense gas through radiation and supernovae is quite important in regulating black hole growth.

## 5 SUMMARY & DISCUSSION

The goal of this paper was to use the large sample of Pop III remnant black holes provided by the *Renaissance* simulations to study both their evolution and growth over the course in the early Universe. The *Renaissance* simulations sample three large-scale galac-

tic environments, span three orders of magnitude in halo mass ( $10^6 M_{\odot} \leq M_{\text{halo}} \leq 10^9 M_{\odot}$ ), provide roughly 300 Myr of black hole evolution time, and form roughly 15,000 Pop III remnant black holes. This mass range allows us to span the boundary between  $\text{H}_2$ -cooling mini-haloes and atomic cooling haloes. We supplement this with 12 Pop III remnants from the extremely high-resolution *Pop2Prime* simulation, in which we disable star formation part of the way through to test the effect of stellar feedback on black hole growth. Our results can be summarized as:

- In all simulations, the vast majority of Pop III remnant black holes grow by negligible amounts, with relative mass gains ranging from  $10^{-16}$  to 0.1. Less than 100 of the 15,000 total black holes grew by more than  $10^{-3}$  of their initial masses, with most of these coming from the Rarepeak (densest region), followed by the Normal (next densest), and just a few from the Void simulation. The instantaneous accretion rates only exceed the Eddington rate one time for one black hole.

- The black holes that grew the most did so within about 10 Myr of their formation, after which time they grew negligibly. All formed from Pop III stars in the mass range where no supernova occurs. These black holes show no preference in host halo mass.

- Clumps of gas with high Bondi-Hoyle accretion rates exist within galaxies, but the instances of black holes existing within them are rare and short-lived. On average, black holes are tens to hundreds of pc away from highly accretable (cold and dense) clumps. These clumps appear to be rapidly destroyed by star formation and feedback before black holes have a chance to accrete significantly from them. In examining the halo hosting the most black holes in the *Renaissance* simulations, most of the instances of black holes located within accretable clumps were newly born and formed without a supernova.

- In the *Pop2Prime* simulations, the average black hole growth increased by more than two orders of magnitude within 100 Myr of turning off star formation. Black holes in haloes that had more time to reassemble after the black hole-forming supernova showed significantly increased growth rates, up to five orders of magnitude. This is due primarily to the increase in gas density.

Overall the *Renaissance* simulations indicate that black holes born from the remnants of Pop III stars never enter regions where rapid and sustained accretion is possible. The early bottleneck which has been previously shown to prevent early black hole growth continues as black holes migrate into more massive haloes, although the halos studied here remain under the minimum mass where [Pelupessy et al. \(2007\)](#) find super-Eddington growth may be

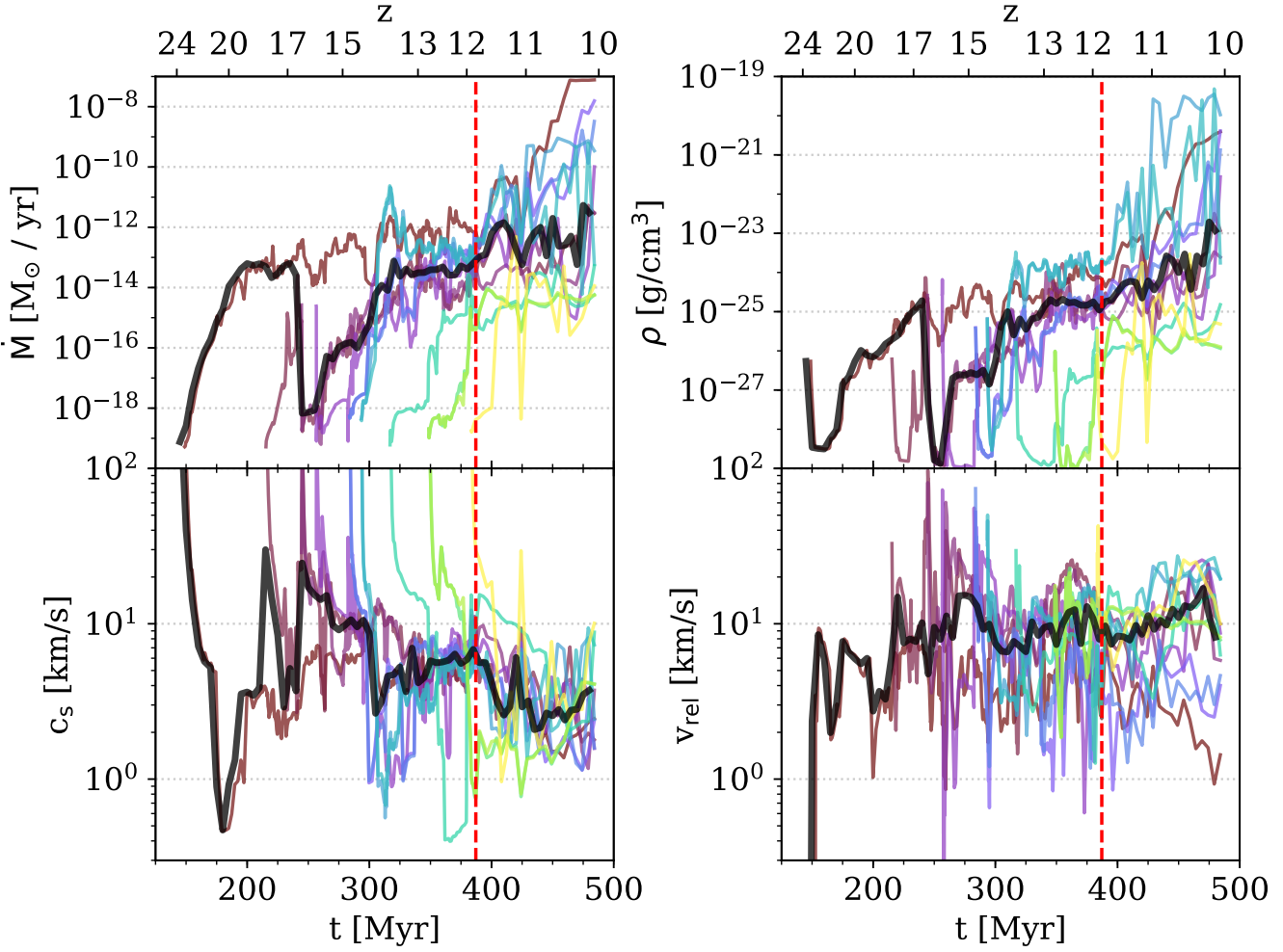


**Figure 9.** Growth histories and associated gas physical conditions for all 12 black holes in the *Pop2Prime* simulation, with median values shown by the thick, black line. The vertical, red dashed line denotes the time when star formation was turned off. *Top-left:* accretion rate. *Top-right:* gas density. *Bottom-left:* local sound speed. *Bottom-right:* relative velocity between gas and particle.

possible. We conclude that black holes born from Pop III remnants in mini-haloes are likely to experience very limited growth in the early Universe. We see no appreciable growth in any black holes in halo masses up to  $10^9 M_{\odot}$ . This provides further evidence of the difficulty of Pop III remnant black holes reaching SMBH scales by  $z = 6$ , although the possibility of doing so in rarer, more massive haloes still exists. This has additional consequences for the formation of intermediate mass black holes (IMBHs). If the Pop III remnants seeds are unable to accrete as cosmic time proceeds in more massive haloes then they will not grow to form a population of IMBHs and may go some way to explaining the relative dearth of IMBHs observed thus far (Koliopanos 2018). It is also possible that over a longer period these black holes will sink to the centre of larger haloes or undergo several interactions with clumps which enable the black hole to grow. However, *Renaissance* does not follow the evolution of structure sufficiently far for us to answer that question. Alternatively, it may also be that periods of high accretion (possibly super-Eddington) can be achieved in metal-free haloes with reduced  $H_2$  fractions rather than in the minihaloes that led to the creation of the black holes examined here. However, *Renaissance* has no prescription to form stars in such environments, though the environments do exist in *Renaissance* (Wise et al. in

prep). Such regions with their deeper potential wells may be more advantageous for forming rapidly accreting black hole seeds which can then go on to become IMBH and/or SMBHs.

A number of other simplifications made in this work or by the simulations studied have the potential to alter the findings presented here. The use of post-processing limits the temporal resolution to the time between snapshots, which here is generally a few Myr. Any events occurring between snapshots will naturally be lost. In particular, this likely leads to an underestimation of the early-time growth of black holes forming without a supernova, i.e., the situation that we find to yield the most growth. As well, any other dynamic effects requiring an accurate calculation of the black hole’s mass evolution during the simulation, such as dynamical friction, cannot be accounted for. The influence of feedback from the accreting black hole on the survival of high accretability clouds is also not clear. Black hole feedback could act similarly to stellar feedback and destroy these clouds, or it may simply delay star formation while largely keeping the cloud in tact. This could potentially give any embedded black holes additional time to grow. Finally, the optically-thin treatment of the LW radiation field may lead to artificially low  $H_2$  fractions in some instances, thus reducing the cooling rate in  $\sim 10^3$  K gas and lowering both the star formation and

black hole growth efficiencies. A significantly higher  $H_2$  fraction could potentially even give rise to thermal instability, which could require the use of a boost factor higher than one for the accretion rate. However, an increase in the cooling would also allow stars to form more readily, which will act to destroy high-accretability gas, making the precise balance unclear. As always, these and any other shortcomings provide ample avenues for further progress.

## ACKNOWLEDGEMENTS

We thank the anonymous referee for their useful comments on the manuscript. BDS is supported by NSF AST-1615848. JAR acknowledges the support of the EU Commission through the Marie Skłodowska-Curie Grant - “SMARTSTARS” - grant number 699941. MLN was supported by NSF AST-1102943 and AST-1615848. BWO was supported in part by NSF grants PHY-1430152 and AST-1514700, by NASA grants NNX12AC98G, NNX15AP39G, and by Hubble Theory Grants HST-AR-13261.01-A and HST-AR-14315.001-A. JHW is supported by National Science Foundation grant AST-1614333, NASA grant NNX17AG23G, and Hubble theory grants HST-AR-13895 and HST-AR-14326. The *Renaissance* and *Pop2Prime* simulations were performed on Blue Waters, operated by the National Center for Supercomputing Applications (NCSA) with PRAC allocation support by the NSF (award number ACI-0832662). The subsequent analysis was performed using time awarded under award number ACI-1514580. This research is part of the Blue Waters sustained-petascale computing project, which is supported by the NSF (award number ACI-1238993 and ACI-1514580) and the state of Illinois. Blue Waters is a joint effort of the University of Illinois at Urbana-Champaign and its NCSA. Finally, this research was made possible by a mountain of open-source scientific software, including Enzo (Bryan et al. 2014), yt (Turk et al. 2011b), Rockstar (Behroozi et al. 2013a), consistent-trees (Behroozi et al. 2013b), and ytree (Smith 2018), sitting on a vast continent of open-source software packages and libraries like Python, matplotlib, and NumPy, just to name a few. We are grateful to everyone who contributed to these projects.

## REFERENCES

- Abel T., Anninos P., Zhang Y., Norman M. L., 1997, *New Astronomy*, 2, 181
- Abel T., Bryan G. L., Norman M. L., 2000, *ApJ*, 540, 39
- Abel T., Bryan G. L., Norman M. L., 2002a, *Science*, 295, 93
- Abel T., Bryan G. L., Norman M. L., 2002b, *Science*, 295, 93
- Agarwal B., Khochfar S., Johnson J. L., Neistein E., Dalla Vecchia C., Livio M., 2012, *MNRAS*, 425, 2854
- Agarwal B., Davis A. J., Khochfar S., Natarajan P., Dunlop J. S., 2013, *MNRAS*, 432, 3438
- Agarwal B., Smith B., Glover S., Natarajan P., Khochfar S., 2016, *MNRAS*, 459, 4209
- Ahn K., Xu H., Norman M. L., Alvarez M. A., Wise J. H., 2015, *ApJ*, 802, 8
- Alvarez M. A., Wise J. H., Abel T., 2009, *ApJ*, 701, L133
- Bañados E. et al., 2018, *Nature*, 553, 473
- Becerra F., Greif T. H., Springel V., Hernquist L. E., 2015, *MNRAS*, 446, 2380
- Begelman M. C., Volonteri M., Rees M. J., 2006, *MNRAS*, 370, 289
- Begelman M. C., Rossi E. M., Armitage P. J., 2008, *MNRAS*, 387, 1649
- Behroozi P. S., Wechsler R. H., Wu H. Y., 2013a, *ApJ*, 762, 109
- Behroozi P. S., Wechsler R. H., Wu H. Y., Busha M. T., Klypin A. A., Primack J. R., 2013b, *ApJ*, 763, 18
- Bondi H., 1952, *MNRAS*, 112, 195
- Booth C. M., Schaye J., 2009, *MNRAS*, 398, 53
- Bromm V., Coppi P. S., Larson R. B., 1999, *ApJ*, 527, L5
- Bromm V., Coppi P. S., Larson R. B., 2002, *ApJ*, 564, 23
- Bryan G. L., Norman M. L., O’Shea B. W., Abel T., Wise J. H., Turk M. J., The Enzo Collaboration, 2014, *ApJS*, 211, 19
- Chen P., Wise J. H., Norman M. L., Xu H., O’Shea B. W., 2014a, *ApJ*, 795, 144
- Chen P., Wise J. H., Norman M. L., Xu H., O’Shea B. W., 2014b, *ApJ*, 795, 144
- Clark P. C., Glover S. C. O., Smith R. J., Greif T. H., Klessen R. S., Bromm V., 2011, *Science*, 331, 1040
- Crosby B. D., O’Shea B. W., Smith B. D., Turk M. J., Hahn O., 2013, *ApJ*, 773, 108
- Devecchi B., Volonteri M., 2009, *ApJ*, 694, 302
- Eisenstein D. J., Hu W., 1999, *ApJ*, 511, 5
- Fan X., Carilli C. L., Keating B., 2006, *ARA&A*, 44, 415
- Fielding D., Quataert E., McCourt M., Thompson T. A., 2017, *MNRAS*, 466, 3810
- Gürkan M. A., Freitag M., Rasio F. A., 2004, *ApJ*, 604, 632
- Gürkan M. A., Fregeau J. M., Rasio F. A., 2006, *ApJ*, 640, L39
- Habouzit M., Volonteri M., Dubois Y., 2017, *MNRAS*, 468, 3935
- Haemmerlé L., Woods T. E., Klessen R. S., Heger A., Whalen D. J., 2018, *MNRAS*, 474, 2757
- Hahn O., Abel T., 2011, *MNRAS*, 415, 2101
- Heger A., Woosley S. E., 2002, *ApJ*, 567, 532
- Hirano S., Hosokawa T., Yoshida N., Umeda H., Omukai K., Chiaki G., Yorke H. W., 2014, *ApJ*, 781, 60
- Hosokawa T., Omukai K., Yorke H. W., 2013a, *ApJ*, 778, 178
- Hosokawa T., Yorke H. W., Inayoshi K., Omukai K., Yoshida N., 2013b, *ApJ*, 778, 178
- Hosokawa T., Hirano S., Kuiper R., Yorke H. W., Omukai K., Yoshida N., 2016, *ApJ*, 824, 119
- Hoyle F., Lyttleton R. A., 1941, *MNRAS*, 101, 227
- Jeon M., Pawlik A. H., Greif T. H., Glover S. C. O., Bromm V., Milosavljević M., Klessen R. S., 2012, *ApJ*, 754, 34
- Jeon M., Pawlik A. H., Bromm V., Milosavljević M., 2014, *MNRAS*, 444, 3288
- Johnson J. L., Bromm V., 2007, *MNRAS*, 374, 1557
- Katz H., Sijacki D., Haehnelt M. G., 2015, *MNRAS*, 451, 2352
- Kim J. h., Wise J. H., Alvarez M. A., Abel T., 2011, *ApJ*, 738, 54
- Koliopoulos F., 2018, *ArXiv e-prints*
- Komatsu E., Smith K. M., Dunkley J., Bennett C. L., Gold B., Hinshaw, 2011a, *ApJS*, 192, 18
- Komatsu E. et al., 2011b, *ApJS*, 192, 18
- Krumholz M. R., McKee C. F., Klein R. I., 2005, *ApJ*, 618, 757
- Latif M. A., Schleicher D. R. G., Schmidt W., Niemeyer J., 2013a, *MNRAS*, 433, 1607
- Latif M. A., Schleicher D. R. G., Schmidt W., Niemeyer J., 2013b, *MNRAS*, 430, 588
- Lupi A., Haardt F., Dotti M., Fiacconi D., Mayer L., Madau P., 2016, *MNRAS*, 456, 2993
- Machacek M. E., Bryan G. L., Abel T., 2001, *ApJ*, 548, 509
- Madau P., Rees M. J., 2001, *ApJ*, 551, L27
- McCourt M., Oh S. P., O’Leary R., Madigan A. M., 2018, *MNRAS*, 473, 5407
- Meece G. R., Smith B. D., O’Shea B. W., 2014, *ApJ*, 783, 75

- Milosavljević M., Couch S. M., Bromm V., 2009, *ApJ*, 696, L146
- Mortlock D. J. et al., 2011, *Nature*, 474, 616
- Nakauchi D., Hosokawa T., Omukai K., Saio H., Nomoto K., 2017, *MNRAS*, 465, 5016
- Nomoto K., Tominaga N., Umeda H., Kobayashi C., Maeda K., 2006, *Nuclear Physics A*, 777, 424
- O'Shea B. W., Norman M. L., 2007a, *ApJ*, 654, 66
- O'Shea B. W., Norman M. L., 2007b, *ApJ*, 654, 66
- O'Shea B. W., Norman M. L., 2008a, *ApJ*, 673, 14
- O'Shea B. W., Norman M. L., 2008b, *ApJ*, 673, 14
- O'Shea B. W., Abel T., Whalen D., Norman M. L., 2005, *ApJ*, 628, L5
- O'Shea B. W., Wise J. H., Xu H., Norman M. L., 2015, *ApJ*, 807, L12
- Pacucci F., Natarajan P., Volonteri M., Cappelluti N., Urry C. M., 2017, *ApJ*, 850, L42
- Pelupessy F. I., Di Matteo T., Ciardi B., 2007, *ApJ*, 665, 107
- Pezzulli E., Valiante R., Schneider R., 2016, *MNRAS*, 458, 3047
- Pezzulli E., Volonteri M., Schneider R., Valiante R., 2017, *MNRAS*, 471, 589
- Regan J. A., Haehnelt M. G., 2009a, *MNRAS*, 396, 343
- Regan J. A., Haehnelt M. G., 2009b, *MNRAS*, 393, 858
- Regan J. A., Johansson P. H., Haehnelt M. G., 2014, *MNRAS*, 439, 1160
- Regan J. A., Johansson P. H., Wise J. H., 2016, *MNRAS*
- Regan J. A., Visbal E., Wise J. H., Haiman Z., Johansson P. H., Bryan G. L., 2017, *Nature Astronomy*, 1, 0075
- Schleicher D. R. G., Palla F., Ferrara A., Galli D., Latif M., 2013, *A&A*, 558, A59
- Shakura N. I., Syun'yaev R. A., 1973, *A&A*, 24, 337
- Smith B., 2018, <https://github.com/brittonsmith/ytree>: ytree version 2.0.2 release
- Smith B. D., Sigurdsson S., 2007, *ApJ*, 661, L5
- Smith B. D., Turk M. J., Sigurdsson S., O'Shea B. W., Norman M. L., 2009a, *ApJ*, 691, 441
- Smith B. D., Turk M. J., Sigurdsson S., O'Shea B. W., Norman M. L., 2009b, *ApJ*, 691, 441
- Smith B. D., Wise J. H., O'Shea B. W., Norman M. L., Khochfar S., 2015, *MNRAS*, 452, 2822
- Springel V., Di Matteo T., Hernquist L., 2005, *MNRAS*, 361, 776
- Sugimura K., Hosokawa T., Yajima H., Inayoshi K., Omukai K., 2018, *MNRAS*, 478, 3961
- Tanaka T., Haiman Z., 2009, *ApJ*, 696, 1798
- Tegmark M., Silk J., Rees M. J., Blanchard A., Abel T., Palla F., 1997, *ApJ*, 474, 1
- Trenti M., Stiavelli M., 2009, *ApJ*, 694, 879
- Turk M. J., Abel T., O'Shea B., 2009a, *Science*, 325, 601
- Turk M. J., Abel T., O'Shea B., 2009b, *Science*, 325, 601
- Turk M. J., Norman M. L., Abel T., 2010, *ApJ*, 725, L140
- Turk M. J., Clark P., Glover S. C. O., Greif T. H., Abel T., Klessen R., Bromm V., 2011a, *ApJ*, 726, 55
- Turk M. J., Smith B. D., Oishi J. S., Skory S., Skillman S. W., Abel T., Norman M. L., 2011b, *ApJS*, 192, 9
- Turk M. J., Oishi J. S., Abel T., Bryan G. L., 2012, *ApJ*, 745, 154
- Valiante R., Schneider R., Volonteri M., Omukai K., 2016, *MNRAS*
- Venemans B. P. et al., 2013, *ApJ*, 779, 24
- Voit G. M., Meece G., Li Y., O'Shea B. W., Bryan G. L., Donahue M., 2017, *ApJ*, 845, 80
- Volonteri M., Silk J., Dubus G., 2015, *ApJ*, 804, 148
- Whalen D., Abel T., Norman M. L., 2004, *ApJ*, 610, 14
- Wise J. H., Abel T., 2007, *ApJ*, 671, 1559
- Wise J. H., Abel T., 2011, *MNRAS*, 414, 3458
- Wise J. H., Turk M. J., Abel T., 2008, *ApJ*, 682, 745
- Wise J. H., Abel T., Turk M. J., Norman M. L., Smith B. D., 2012, *MNRAS*, 427, 311
- Wise J. H., Turk M. J., Norman M. L., Abel T., 2012a, *ApJ*, 745, 50
- Wise J. H., Turk M. J., Norman M. L., Abel T., 2012b, *ApJ*, 745, 50
- Wise J. H., Demchenko V. G., Halicek M. T., Norman M. L., Turk M. J., Abel T., Smith B. D., 2014, *MNRAS*, 442, 2560
- Wolcott-Green J., Haiman Z., Bryan G. L., 2011, *MNRAS*, 418, 838
- Woods T. E., Heger A., Whalen D. J., Haemmerlé L., Klessen R. S., 2017, *ApJ*, 842, L6
- Woosley S. E., Weaver T. A., 1995, *ApJS*, 101, 181
- Wu X. B. et al., 2015, *Nature*, 518, 512
- Xu H., Wise J. H., Norman M. L., 2013a, *ApJ*, 773, 83
- Xu H., Wise J. H., Norman M. L., 2013b, *ApJ*, 773, 83
- Xu H., Ahn K., Wise J. H., Norman M. L., O'Shea B. W., 2014, *ApJ*, 791, 110
- Xu H., Norman M. L., O'Shea B. W., Wise J. H., 2016a, *ApJ*, 823, 140
- Xu H., Wise J. H., Norman M. L., Ahn K., O'Shea B. W., 2016b, *ApJ*, 833, 84
- Yoshida N., Abel T., Hernquist L., Sugiyama N., 2003, *ApJ*, 592, 645